Cement and Concrete Composites 118 (2021) 103956

Contents lists available at ScienceDirect

Cement and Concrete Composites

journal homepage: http://www.elsevier.com/locate/cemconcomp

Mechanical properties and self-healing capacity of Ultra High Performance Fibre Reinforced Concrete with alumina nano-fibres: Tailoring Ultra High Durability Concrete for aggressive exposure scenarios

Estefania Cuenca [a,*], Leonardo D'Ambrosio [a], Dennis Lizunov [b,c], Aleksei Tretjakov [b,c], Olga Volobujeva [d], Liberato Ferrara [a]

[a] Department of Civil and Environmental Engineering, Politecnico di Milano, Italy
[b] ANF Development, Tallinn, Estonia
[c] now at ANF Technology Ltd, London, United Kingdom
[d] Department of Material and Environmental Technology, Tallinn University of Technology, Tallinn, Estonia

ARTICLE INFO

Keywords:
Self-healing
Crystalline admixtures
Alumina nano-fibres
Durability
Ultra High
Durability Concrete

ABSTRACT

The effects of alumina nano-fibres are investigated in this paper on the mechanical performance of Ultra High Performance Fibre Reinforced Cementitious Concrete and their efficacy in enhancing the durability of the cementitious composite when exposed to extremely aggressive conditions, with main reference to the stimulated autogenous crack sealing and self-healing capacity. A tailored characterization of the flexural and tensile behaviour of the composite has been first of all performed, also with the purpose of validating an experimental and analytical approach for the identification of the tensile stress vs. strain/crack opening constitutive relationship, which makes use of a purposely conceived indirect tensile test methodology, called Double Edge Wedge Splitting test. Secondly the crack sealing and self-healing capacity have been investigated, considering the recovery of both mechanical flexural performance and durability properties (water permeability) and cross analysing the results for a thorough validation. Microstructural investigations have complemented the aforementioned experimental programme to confirm the efficacy of alumina nano-fibres in enhancing the durability performance of the investigated composites. Superior performance of the mix with alumina nano-fibres with respect to parent companion ones has been highlighted and explained through both a nano-scale reinforcing effects which helps in controlling the cracking process since its very onset as well as through their hydrophilic nature which is likely to foster cement and binder hydration reactions, which can usefully stimulate crack sealing and performance healing recovery at both the macroscopic and mesoscopic fibre-matrix interface) level.

1. Introduction

Opportunities and benefits deriving from implementing nanotechnology approaches, methods, processes and products in the field of construction [1] have been attracting researchers in academia and industry for a least a couple of decades, also as a challenging innovation driver in a sector which, though accounting for an average 6% of the world GDP, still suffers from a lag in innovation uptake.

As responsible of the production and use of the second most largely used material on the planet, the first being water, the "concrete community" has been continuously bringing remarkable contributions in the field, also able to introduce breakthrough conceptual developments into the field and steering future advances towards previously unexplored directions.

As a matter of fact, one of the most common and successfully widespread applications of nanotechnology in the concrete sector has been so far, as from an educated survey of the abundant existing literature, the use of nano-scale constituents into the mix-design of concrete and cement-based composites. Benefits are evident, due to the possibility of achieving higher and higher degree of compaction of the inherently porous concrete matrix, with related positive outcomes in terms of reduction of the transport properties and improvement of the

* Corresponding author.
E-mail address: estefania.cuenca@polimi.it (E. Cuenca).

https://doi.org/10.1016/j.cemconcomp.2021.103956
Received 20 August 2020; Received in revised form 13 December 2020; Accepted 20 January 2021
Available online 26 January 2021
0958-9465/© 2021 The Authors. Published by Elsevier Ltd. This is an open access article under the CC BY-NC-ND license (http://creativecommons.org/licenses/by-nc-nd/4.0/).

durability of the un-cracked material. Moreover, the higher specific surface of the employed nano-constituents, with nano-silica covering so far the largest share, their potential reactivity (*e.g.* pozzolanic activity) as well as their widely assessed capacity of acting as nucleation seeds for the hydration of coarser cement and cement substitutes binding particles have also resulted into enhancement of the mechanical properties, mainly compressive strength, but also of the bulk transport properties, thus inferring higher durability [2,3].

It is by the way worth remarking that improvements in mechanical properties, and most of all if they are referred to compressive strength alone, have to be carefully evaluated with reference to their effective "structural exploitability". For example, the increase in compressive strength cannot always lead to a proportional reduction of the cross-section dimensions of a compressed member, since buckling failure may at a certain point become dominant with respect to strength failure mode.

Opportunities for using nano-sized reinforcement were also explored [4,5] mainly in the form of carbon nano-fibres and nano-tubes [6], as well as of cellulose nano-fibres, which, besides working out their reinforcement effect at the size of the very crystalline structure of the material, have also proved effective in providing additional functionalities, including, *e.g.*, enhanced corrosion resistance [7] self-curing and self-sensing ability [8,9], while also being able to upgrade durability in cracked state [10], e.g. fostering and enhancing autogenous self-healing capacity [11].

Latest developments in this field include the use of graphene nano-platelets and graphene oxide, able to provide enhancement due to both nano-filling and nano-reinforcing effects but at even much lower loading than other "conventional" nano-constituents [12], provided, like for all other nanoparticles, tailored methods are adopted to adequately disperse and stabilize it into alkaline cementitious solutions [13]. Possibilities of using graphene oxide as a coating material for fibre treatment, exploiting its interaction with cement hydrates in enhancing the overall performance of the composites have been also recently explored [14,15].

The aforementioned developments in the use of nano-sized constituents in cementitious composites are opening a new breakthrough "metamaterial" based approach to the concept, design, fabrication testing and validation up to the structural application scale of cement-based construction materials [16]. Thanks to the effects of such constituents on the material microstructure and on its development and evolution under different potential scenarios, it is becoming possible to effectively govern the chemical reactions and processes which are responsible for the evolution of the material performance over time and in aggressive scenarios [17].

Steric modification in material microstructure but also in the structural response of the material to the anticipated service stress states may change the boundary conditions of the aforementioned reactions and processes can be slowed down, their negative effects being likely counteracted by positive ones due to, *e.g.*, the continuous microstructure evolution and improvement thanks to healing. Moreover, the same processes can result into the formation of different, and differently – if not less – harmful reaction products, as it may happen to corrosion reactions if crack widths are permanently kept below a certain threshold [18].

High performance Fibre Reinforced Concrete and Cementitious Composites have a highly compact meso- and micro-structure, characterized by extremely low porosity and a strain-hardening tensile behaviour. The latter is characterized by stable formation, up to very high deformation levels, of multiple tiny cracks (up to tens of microns). Moreover, the peculiar material composition is highly conducive to effective autogenous healing, further benefiting from the multiple cracked state. All these features pave the way for an effective development and implementation of the innovative breakthrough approach of durability-based material concept and design [19–22].

In this framework, the consortium of the H2020 project ReSHEALience (GA 760824) has been actually working to the concept formulation and validation of Ultra High Durability Concrete (UHDC) meant as an upgrade of the UHPFRCC concept, and aimed at obtaining through tailored nano-constituents and their synergy with autogenous and stimulated healing mechanisms an enhanced durability in the cracked state, which represents the actual structural serviceability state, also under extremely aggressive conditions [23]. The group led by the senior author of this paper has already performed a preliminary investigation on the effects of selected nano-constituents (alumina nano-fibres and cellulose nano-fibrils and nano-crystals) in enhancing, also in synergy with crystalline admixtures, the autogenous healing capacity of UHPFRCC mixes, conceived for applications in chemically aggressive environments (water tanks in a geothermal power plant) [24]. Positive results obtained from the study cited above have led to have a deeper understanding on the role of each single nano-constituent, the present investigation focusing on alumina nano-fibres as a quite new product in the field of concrete and advanced cement based materials technology.

Alumina nano-fibres, when added at less than 1% by weight of cement, have been shown to have beneficial effects on the compressive strength [25–28], when employed, e.g. in HPFRCC type mixes, with either polyethylene or poly-vinyl-alcohol fibre reinforcement, they also guaranteed enhanced flexural strength and deformation capacity. Use into oil well slurries has been also documented, where, besides moderate improvement also in splitting tensile strength, the stability of the rheological performance upon their incorporation was also studied. The mechanisms of performance enhancement due to the addition of alumina nano-fibres has been explained in a twofold manner. On the one hand alumina nano-fibres, which contain free hydroxyl groups on their surface, act as nucleation site for hydration of cement particles. On the other hand, because of their size, aluminium oxide nano-fibres can act as reinforcement of the layered CSH structure thus reducing the shrinkage deformation and providing a nano-structural toughening effect. In all cases, the need has been highlighted to provide a suitably dispersed suspension to be easily handled with the mixing procedure as well as to guarantee the compatibility with the employed superplasticizer.

In this study a thorough characterization has been performed of the mechanical performance of UHPFRCCs containing NAFEN ® alumina nano-fibres. Flexural tests on beams with two different depths have been employed, together with tailored Double Edge Wedge Splitting (DEWS) indirect tensile tests [29], which has been demonstrated able to yield straightforward the tensile stress vs. crack opening constitutive relationship of the strain-hardening fibre reinforced cementitious composite [30]. On the one hand, the effects were checked of alumina nano-fibres on the strain hardening capacity of the material. At the same time the effectiveness was assessed of the employed multi-test experimental procedure, coupled with back analysis of the flexural tests performed assuming in input the results of DEWS indirect tensile tests. In addition, a characterization of the self-healing capacity of the "nano-additioned" composite was performed, both with reference to the recovery of the water flow permeability as well as of the mechanical performance, in both cases complemented with an image analysis of the crack closure. Crosswise analysis of the results of the present investigation will be enriched by a thorough micro-structural characterization of the bulk material as well as of the healing/healed crack regions. Moreover, the comparison with the results of analogous experimental campaigns performed on companion UHPFRCC/UHDC mixes cast without the alumina nano-fibres and even without the crystalline self-healing stimulator or with different types of cements, which stands as a unique feature of this study will also allow to have a deeper insight, also quantitative, into the performance enhancement brought by the employed nano-constituents as well as on the reliability of the whole methodology employed for the assessment of the mechanical and healing performance.

Table 1
Mix composition of the investigated UHPFRCC/UHDC (dosages in kg/m^3).

Constituents	kg/m^3
Cement CEM I 52.5R	600
Slag	500
Water	200
Steel fibres (l_f = 20 mm; d_f = 0.22 mm)	120
Sand (0–2 mm)	982
Superplasticizer	33
Crystalline admixtures	4.8
Alumina nano-fibres [0.25% by cement mass]	1.5

2. Materials

The mix composition of the UHPFRCC/UHDC employed in this study is shown in Table 1. The parent UHPFRCC mix with no healing crystalline admixture and no alumina nano-fibre addition has been extensively studied by Ferrara et al. [29,31–35] with respect to both the characterization of the mechanical performance and related identification of the tensile constitutive stress vs. crack opening behaviour and of the autogenous self-healing capacity as well. The composition of the employed cement (CEM I 52.5R) and slag are reported in Table 2 whereas Table 3 summarizes the grain size distribution of the crushed sand employed as fine aggregate in the mix. Straight steel fibres 20 mm long and with a diameter equal to 0.22 mm have been employed at a volume ratio equal to 1.5%, this being deemed as instrumental at achieving the level of strain hardening, in terms of strength and deformation capacity required by the intended application [24,30].

The mix composition served as a reference to upgrade the UHPFRCC concept to that of Ultra High Durability Concrete (UHDC) in structures exposed to chemically aggressive environments. To this purpose, and with the specific aim of employing the material at issue in basins collecting water from the cooling towers (water temperature around 30 °C) in geothermal power plants, as a pilot demonstration of the H2020 ReSHEALience project [23,24] where the aggressive conditions is represented by the high sulphate and chloride contents of the fluids, the reference mix composition, which features a high volume replacement of cement by slag right for stability under sulphate rich waters, has been further "engineered" as follows:

- first of all, a crystalline admixture (CA) has been added, as stimulator of the autogenous healing capacity [36,37] and also able to develop synergy with the fibre reinforcement through improved fibre-matrix bond [38,39]. CA is composed of particles of irregular shape with sizes ranging from 1 to 20 μm being present calcium, oxygen, silicon, magnesium, aluminium and potassium among other chemical elements. When CA is added into the concrete, the ability of concrete to self-heal and self-seal is stimulated. When concrete is exposed to humidity/water, the chemical reaction is activated, also thanks to the hydrophilic nature of the CA, resulting in the formation of insoluble needle-like crystals in all hairline cracks, pores and capillaries throughout the entire concrete matrix. An extensive characterization of the mechanical and healing performance of the mix containing the crystalline admixture has been performed and reported by Refs. [11,30];
- alumina nano-fibres have hen been added, at a dosage equal to 0.25% by weight of cement, as from a previous mix validation study reported by Cuenca et al. [11].

Table 3
Grain size distribution of the employed sand.

Sieve diameter (mm)	0.2	0.35	0.45	0.60	1.00	1.50	2.00
Passing %	14.6	24.3	34.1	43.8	63.5	81.7	100

The alumina nano-fibres (NAFEN ®) employed in this investigation have been provided in a 10% concentration aqueous suspension. These alumina nano-fibres have lengths ranging between 100 and 900 nm and diameters between 4 and 11 nm, to which a specific surface area equal to 155 m^2/g corresponds. Fig. 1 shows some micrographs of alumina nano-fibres, this analysis was performed with a high-resolution scanning electron microscope (HR-SEM Zeiss Merlin). Measurements were made at operating voltage of 15 kV. It is worth remarking that with such a concentration the required nano-fibres amount (1.5 kg/m^3 in the case at issue) come in a suspension which also accounts for about 7% of the total water, which was obviously, as per mix design in Table 1, deducted from the free added water. Suspension concentrations at which the same product is normally employed in other industrial sectors and applications, from aircraft application to the construction of composite sailing and motor yachts [40–44], typically equal to 2% of nano-fibres, would have implied an amount of water in the suspension equal to about 1/3 of the total mixing water. This, also due to the viscosity of the suspension, would have results into hard if not impossible mixing of the cementitious composite. With reference to this, and also in order to guarantee a proper dispersion of the nano-fibres in the composite, the mixing protocol reported in Table 4 has been strictly followed. The higher concentration of the alumina nano-fibres suspension was obtained through an ultrasonic dispersion and disintegration multi-step treatment process; the suspension was further stabilized through a poly-carboxylate sodium silicate admixture. Ultrasonic and disintegrator processors effectively generate nano-sized material slurries, dispersions, and emulsions due to de-agglomeration and the mechanical effects of ultrasonic cavitation. In the case of this research, alumina nano-fibres needed approximately 5 min of ultrasonic treatment per 1 kg of dispersion. Colloidal behaviour of the alumina nano-fibres in water and their electrophoretic mobility can be found in Ref. [45]. The purity and composition of the employed suspension of alumina nano-fibres is confirmed by the results of a TGA analysis shown in Fig. 2.

3. Experimental programme: tests and analysis methods

A thorough experimental programme has been performed with the purpose of providing a comprehensive characterization of the mechanical performance and an assessment of the healing capacity of the investigated mix. The rationale of the programme is summarized in Fig. 3.

For the characterization of the mechanical performance of the composite, besides measuring he compressive strength on 100 mm side cubes, 4-point bending tests on 100 mm deep and 25 mm thin beams, both 100 mm wide and 500 mm long, have been performed. The set-up employed for both specimens is shown in Fig. 4. The specimen, supported over a 450 mm span, has been subjected to two symmetrically positioned point loads, with mutual distance between the two loading points and between each loading point and its closest support equal to 150 mm. Tests have been performed under displacement control, at a speed equal to 3 μm/s for deep beams and 15 μm/s for thin ones. The Crack Opening Displacement (COD), intended as the integral/cumulative measurement of the multiple cracking expected in the central

Table 2
Chemical composition of the employed cement and slag. (LOI: loss on ignition @1000 °C).

Oxide (wt.%)	CaO	SiO_2	Al_2O_3	MgO	SO_3	Fe_2O_3	TiO_2	Mn_2O_3/MnO	K_2O	Na_2O	Other	LOI
PC	59.7	19.5	4.9	3.3	3.4	3.5	0.2	0.1	0.8	0.2	0.4	2.5
BFS	39.2	38.9	10.2	6.4	1.3	0.4	0.6	0.3	0.5	0.8	0.3	1.2

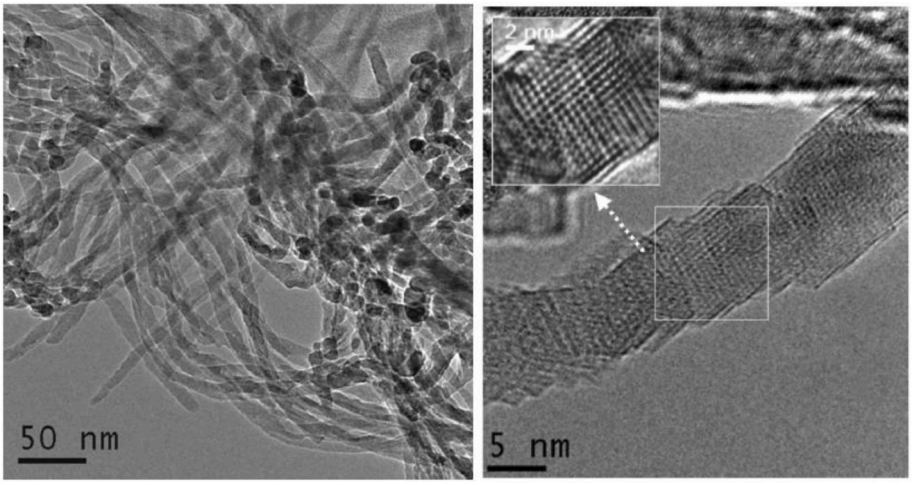

Fig. 1. Microscope images of employed alumina NAFEN ® nano-fibres.

constant bending moment region of the specimen, was measured over a 200 mm length across the central zone of each specimen and on both its sides. Moreover, the net mid-point deflection was measured, employing two symmetrically located LVDTs, as also shown in Fig. 4.

Six tests on prismatic beams were performed, four of them according to a monotonic load path and two of them following a loading/unloading cyclic protocol at 0.5 mm COD intervals. This test allowed to calibrate the evolution of the loading/unloading stiffness and hence of a scalar damage variable through which the calibration of the healing pre-cracking/recycling protocol was also possible.

For flexural tests on thin beam specimens, eight tests were performed, two of which following the loading/unloading cycles as above and the remaining six tested monotonically.

Table 4
Mixing protocol.

Time (min)	Operation
0–2	Dry mixing of cement, slag, CA and sand
2–3	Add water, superplasticiser
3–4	Add ANF suspension
4–19	High speed mixing
19–20	Add fibres
20–23	High speed mixing

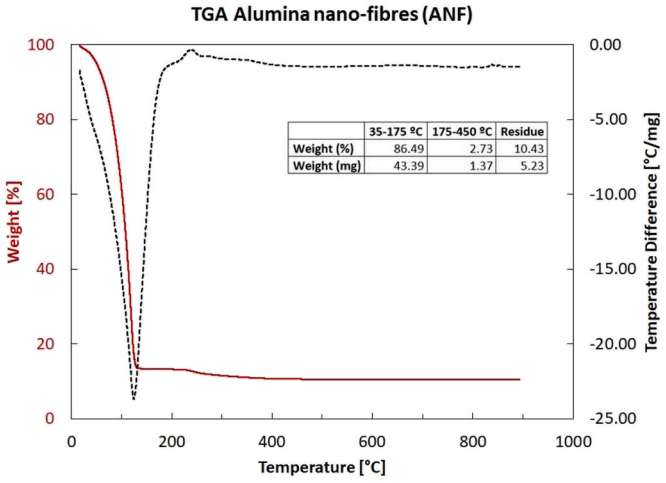

Fig. 2. TGA analysis results of a sample of alumina nano-fibres aqueous suspension as employed in the composition of the investigated UHPFRCC/UHDC mix.

It is worth here remarking that thin specimens were obtained by cutting 1 m long x 0.5 m slabs, which were cast pouring the fluid mix at the centre of one short side of the mould and allowing it to glow, thanks to its self-compacting/self-levelling consistency, along the long side of the same mould until complete form filling, which occurred successfully without any external human or mechanical intervention. This results in some likely alignment of the fibres along the flow, which may have also depended on the actual position of the specimen within the larger slab, as it will be further elucidated in the forthcoming sections of this paper.

At the end of the monotonic flexural tests on thin beams, from the edge undamaged portions of the specimens, 100 mm side "tile-like" samples were obtained which were then further worked out by cutting grooves and notches to obtain the geometry shown in Fig. 5 as well, employed to perform the indirect tensile test named as Double Edge Wedge Splitting (DEWS) test [29]. As already assessed in previous and ongoing studies [37] the test is able to yield in a straightforward manner the tensile stress vs. crack opening constitutive relationship of the cementitious composites. This issue has been also assessed in this paper by comparing the results from DEWS tests with those obtained through a tailored inverse analysis procedure of the flexural test results on the beam tests parent of the DEWS tile samples. It is well known that fibres mainly align along the mix flow direction [29,31,33]. To further check and assess the dependence between the fibre alignment and the tensile behaviour of the material, the specimens were made with a particular geometry. To this purpose, the notch and groove cutting was performed in such a way that the resulting ligament cross sections resulted either parallel or orthogonal to the mix-flow direction. The ligament is going to be subjected to the pure mode I tensile stress state generated by the test set-up. Hence, it is expected to respectively yield a tensile strain softening (fibres parallel to the fracture ligament cross section) or hardening behaviour (fibres orthogonal to the fracture ligament cross section).

The test was performed in displacement control, at a speed equal to 0.5 μm/s, according to the set-up shown in Fig. 6, where it can be seen that the crack opening was measured at two positions along the ligament height on the front face of the specimen and at mid-height of the ligament on the rear. As a whole, twelve DEWS tests were performed, six per each ligament vs. fibre alignment combination.

All the flexural and indirect tensile tests were performed on specimens having been cured more than 2 months after casting in a moist room at 95% RH and 20 °C. The whole mechanical characterization testing activity lasted for about 1 month.

For the self-healing performance assessment both mechanical and durability tests were performed. For the latter, the influence of the crack sealing on the water permeability was checked performing water permeability tests on sound, pre-cracked and healed disks having a

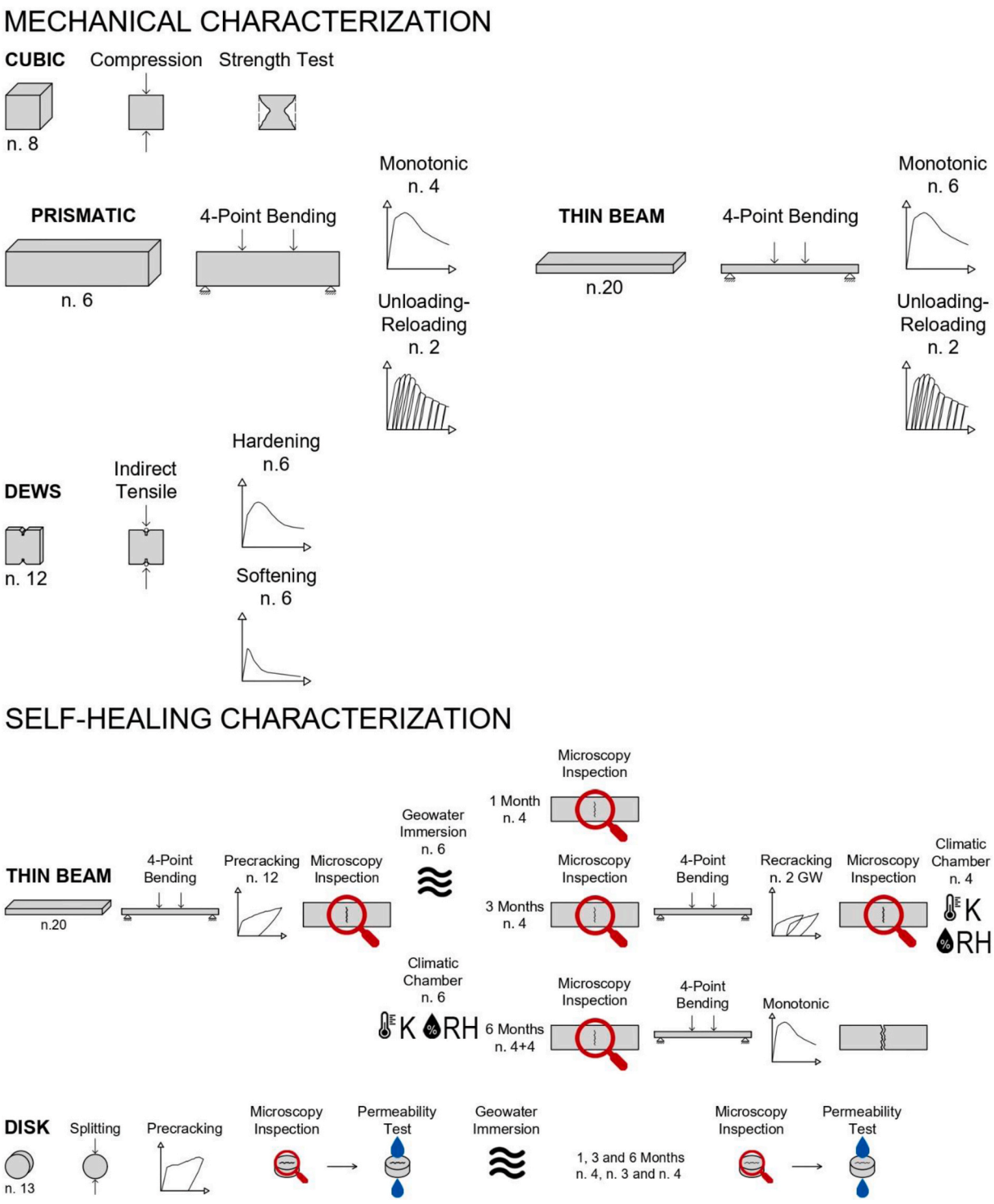

Fig. 3. Rationale of the experimental programme: mechanical characterization.

diameter equal to 100 mm and a thickness of 40 mm. Disks were pre-cracked in splitting, according to the set-up shown in Fig. 7, up to a maximum crack opening equal to 100 μm, variability into residual crack opening ranging from 50 μm to 150 μm, with an average value of 105 μm and a standard deviation equal to 40 μm.

At the end of the pre-cracking the crack was imaged by means of a digital microscope on both sides of the disk and according to an image analysis procedure detailed in Ref. [37] both the initial total crack area $A_{crack,0}$ and the initial average crack width $w_{crack,0}$ were quantified.

After the pre-cracking, water-flow test was performed according to the set-up shown in Fig. 8. The quantity of water flowing through the crack was measured along a time interval of 3 h, at 5 min interval in the first half hour, every 10 min until the first hour, every 20 min until the second hour and every half an hour thereafter. From the water flow vs. time diagrams, a flow rate coefficient K_0 was obtained by means of a suitable fitting. After this, the specimens were kept immersed in geothermal water at laboratory temperature, whose composition in shown in Table 5, for healing and permeability tests were performed again after one, three and size months healing, obtaining the values of permeability coefficient K_t at different scheduled healing times. At the

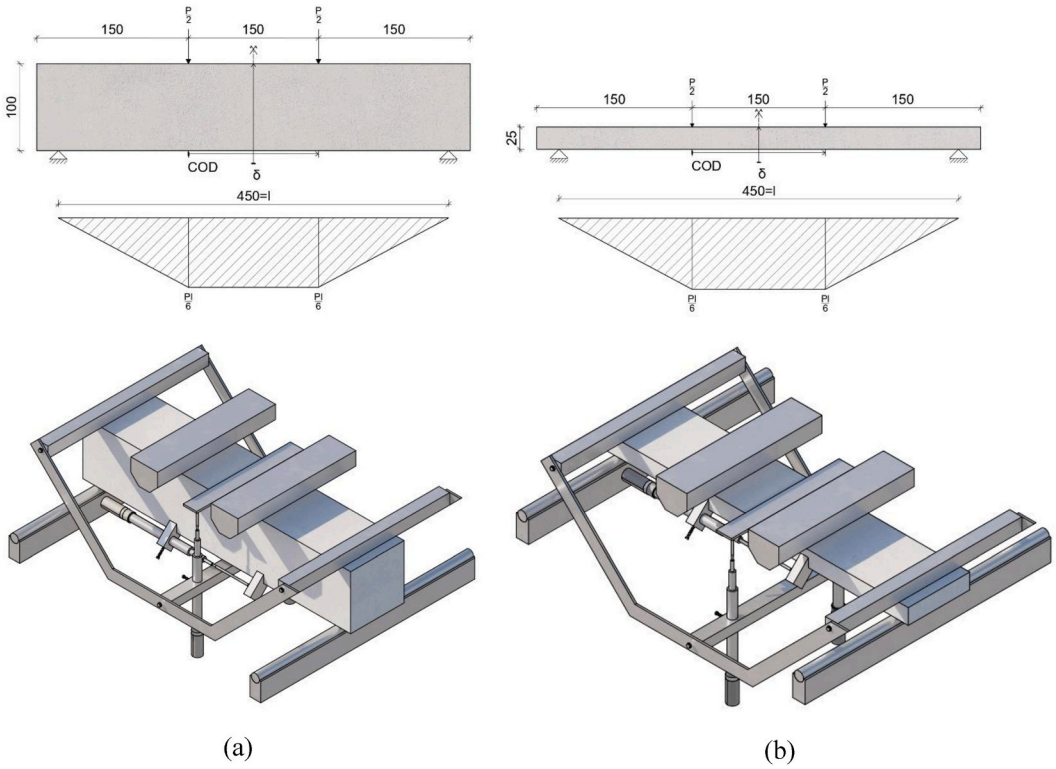

Fig. 4. Schematic and 3D rendering of the 4-point bending test set up on 100 mm deep (a) and 25 mm thick (b) prismatic beam specimens (all dimensions in mm).

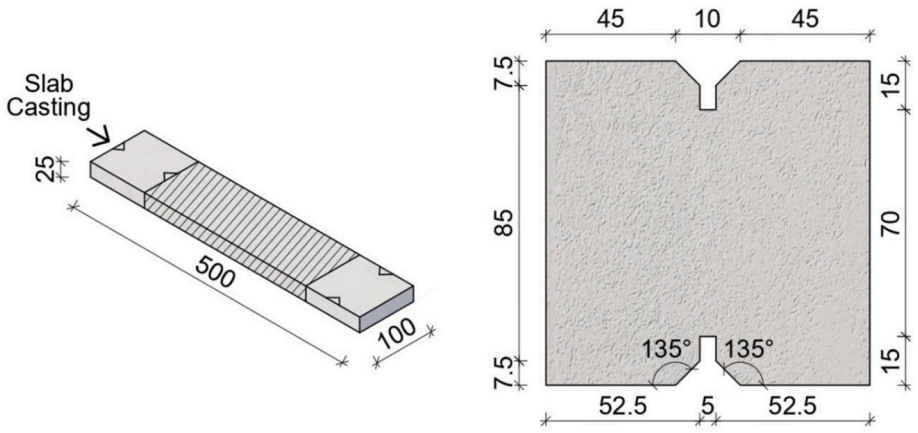

Fig. 5. DEWS specimens cutting from thin beams and detailed geometry (dimensions in mm).

same deadlines, visual imaging of the cracks was also performed on either face of the disk (Fig. 9), obtaining, similarly to what explained above for the pre-cracking stage, the crack area and the average crack width at scheduled healing deadlines, $A_{crack,t}$ and $w_{crack,t}$ respectively, calculating average values between measurements on the top and bottom face of the disk.

From the crack geometry parameters and permeability test results measured as above the following indices of crack sealing and permeability healing were calculated:

$$\text{Index of Crack Sealing ICS} = 1 - \frac{A_{crack,t}}{A_{crack,0}} \quad (1)$$

$$\text{Index of Permeability Healing IPH} = 1 - \frac{K_t}{K_0} \quad (2)$$

The assessment of the healing performance by means of mechanical tests and hence through the effects of healing on the recovery of the mechanical performance was performed as follows, employing twelve thin beam specimens obtained from the two cast large slabs (1 m × 0.5 m) and not already employed for the mechanical time zero performance characterization.

The twelve specimens were all pre-cracked in four point bending up to a 250 μm residual crack opening characterization, the target residual crack opening being quite successfully achieved, with limited variability, thanks to the unloading stiffness calibration performed as above (Fig. 10a). At the end of the pre-cracking process, cracks were mapped with a digital microscope (Fig. 9a), as already explained for the specimens employed for permeability tests, the crack area and the average crack width were calculated and denoted as $A_{crack,0}$ and $w_{crack,0}$ as above. In order to thoroughly and completely map the crack over the whole specimen width, 90 images were acquired, which were subsequently analysed and reassembled through the digital analysis imaging software

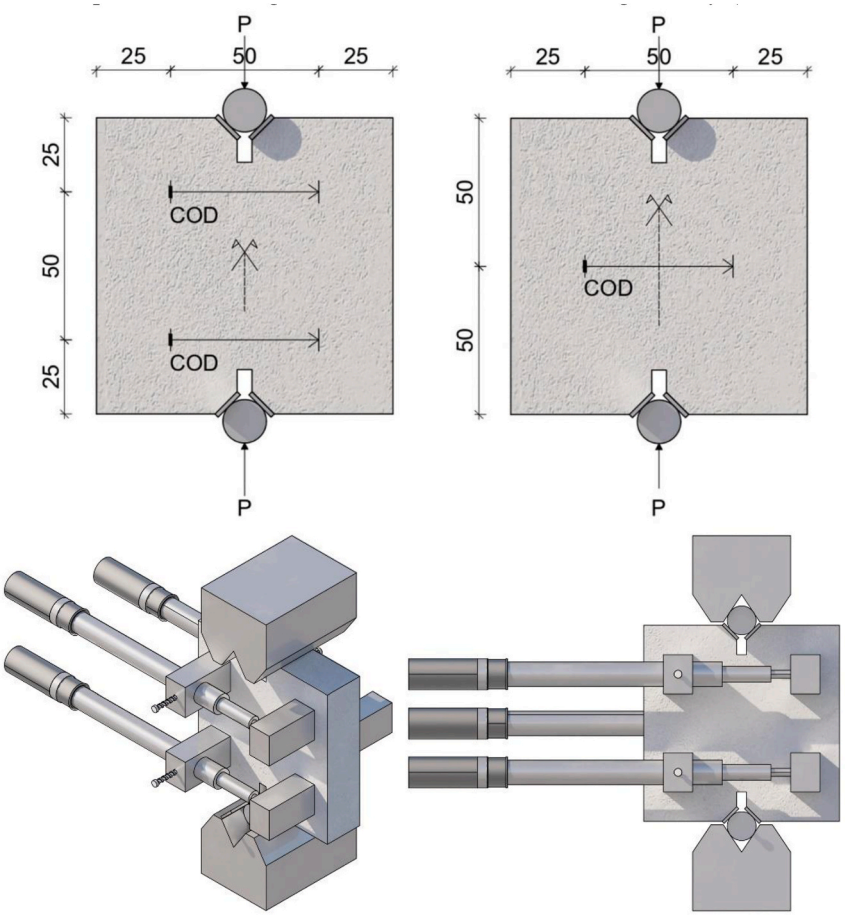

Fig. 6. Schematic of the DEWS tests set-up (dimensions in mm).

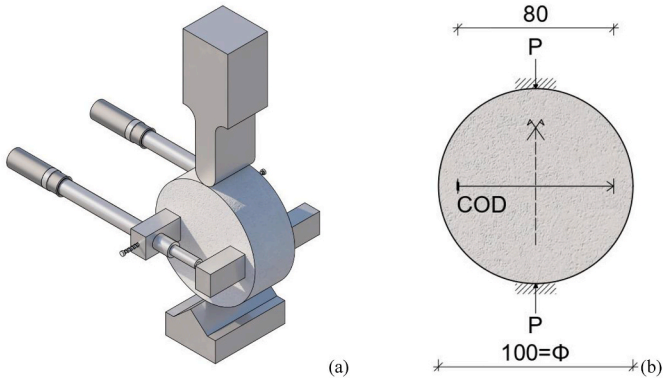

Fig. 7. Schematic of the splitting set-up to pre-crack disks for permeability tests and distribution of obtained residual crack openings (dimensions in mm).

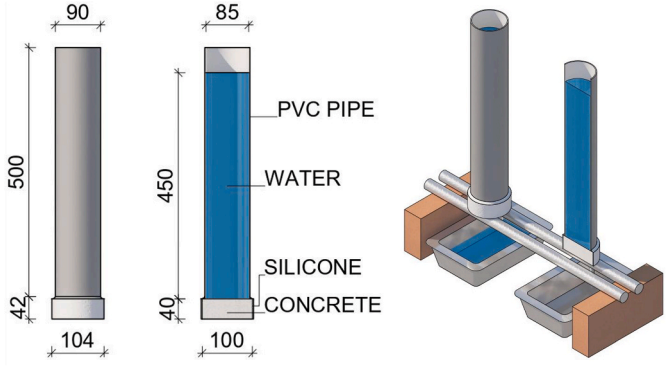

Fig. 8. Schematic and 3D rendering of the water permeability test set-up (dimensions in mm).

Photoshop ® (Fig. 9b).

The twelve specimens were then cured/healed: six of them in a moist room at 20 °C and 95% RH and six immersed in the same geothermal water as above for the water-flow test specimens. At the end of the first month four specimens, two healed in moist room and two in geothermal water, were visually observed for crack sealing and then tested to failure. The remaining eight specimens were once again mapped after three months healing and for of them were re-cracked up to an additional 250 μm residual COD. Altogether the remaining specimens, four re-cracked after three months and four keeping the original initial pre-cracking, were healed up to six months. At the end of this period, all specimens were visually observed for crack sealing and then tested to failure.

At intermediate re-cracking or failure tests, the mechanical performance in terms or load bearing capacity and reloading stiffness was (re) assessed and healing indices, namely the index of stress capacity recovery and the index of stiffness/damage recovery were calculated as hereafter detailed and also explained in Fig. 11. Through the comparison between specimens which benefited of an intermediate monitoring during their healing period and specimens which were only monitored at the end of it, an assessment of the kinetics of the healing was also possible, in case as also affected by the intermediate re-cracking.

The aforementioned programme has been complemented with a thorough micros-structural analysis of the investigated composites.

Table 5
Composition of the geothermal water employed for specimen curing and healing.

Constituent	Al	Ca	Fe	K	Mg	Na	S	Si	SO_4^{2-}	Cl
ppm	0.2	4	0.13	19.8	0.3	1243.2	1523.4	0.3	2678	441

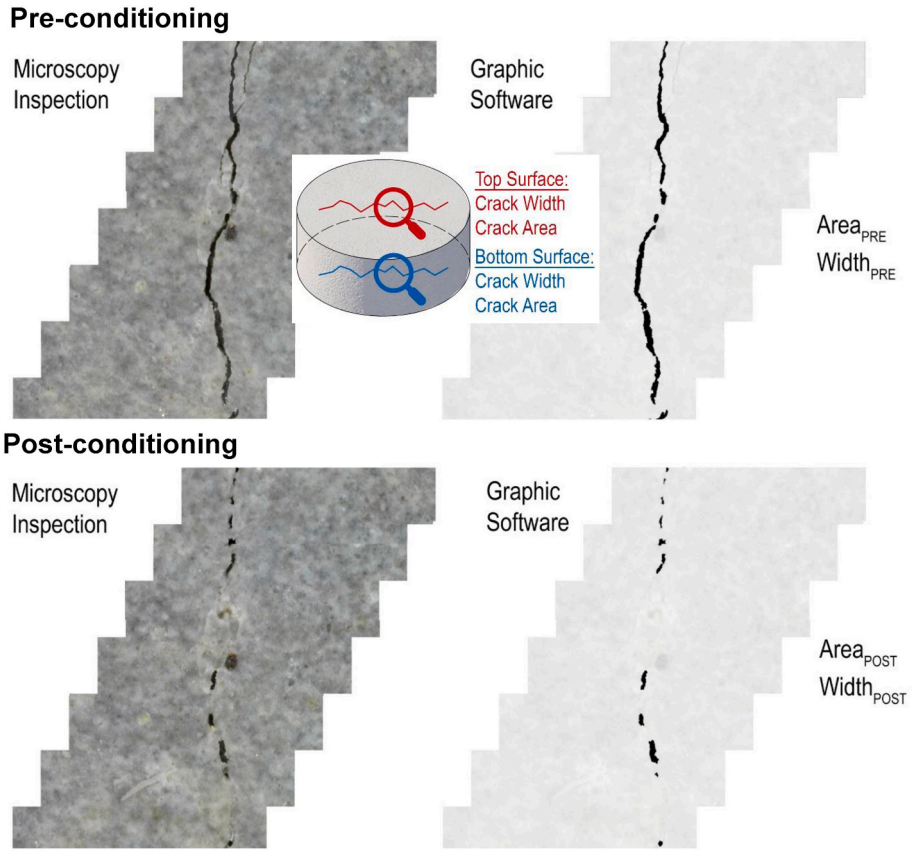

Fig. 9. Visual imaging of the cracks.

Thermogravimetric analysis (TGA) was carried out for the alumina nano-fibre suspension, as in section 2 as well as to study the changes in hydration products caused by the presence of alumina nano-fibres and by the curing condition: climate room (20 °C, 50% RH) and immersion in geothermal water (GW). Concrete samples were ground using a mortar and pestle to obtain powdered homogeneous samples; steel fibres were separated by means of a magnet. Consequently, thermal reduction properties of the samples were characterized by an SDT Q600 V20.9 Build 20 thermal gravimetric analyser under nitrogen flow at 100 ml/min. Temperature was elevated at a constant heating rate of 10 °C/min between 35 and 1450 °C. Temperature was held constant at 105 °C for 2 h to promote elimination of free water.

In this respect, also in order to understand if and how the mix compositions and the healing/exposure conditions did interact with the formation of the crystalline structure, SEM/EDS and XRD analyses were performed on samples both with and without the alumina nano-fibres and exposed to both geothermal water and laboratory environment. To this purpose tests were performed on samples after 6 months curing in climate room (20 °C and 50% RH) and after same time immersion in geothermal water. XRD test was performed to determine the crystalline phases. Tests were carried on powdered concrete using a Bruker D8 Advance instrument with Cu-Kα radiation and a nickel filter. The tests were conducted with a step size of 0.0260° and a counting time of 0.5 s/step, from 5° to 65° 2θ.

4. Experimental results

4.1. Mechanical behaviour and identification of the stress vs. crack-opening relationship

Nominal flexural stress vs. Crack Opening Displacement (COD) curves as obtained from 4-point bending tests on both 100 mm deep and 25 mm thick beams are shown in Fig. 12 a-b respectively. A wider scattering of the performance in the latter case can be observed, also confirming findings of previous related studies [30] which can be explained due to the fact that the thin beams have been obtained from larger slabs and that the local fibre dispersion, and hence the resulting mechanical performance, may have been affected by local flow turbulences and hindrances as due to the pouring of the mix and boundary conditions. Thickness of the specimens have also an obvious effect in forcing planar orientation of the fibres rather than random 3D orientation, in thin vs. deep beams respectively, which also resulted, in the former case as compared to the latter, in a higher (about 10%) peak flexural strength and higher deformation capacity (thin beams: $\sigma_{n,max} = 19$ $COD_{\sigma n,max} = 8.5$, deep beams $\sigma_{n,max} = 17$ $COD_{\sigma n,max} = 8$).

The well-known effects of the orientation of the fibres on tensile behaviour of the material, as also affected by the position of the specimens with respect to the geometrical characteristics of the casting flow, has been also confirmed by the results of DEWS tests, shown in Fig. 13.

It is worth remarking that, as already explained above, when pre-ordaining through notch and groove cutting the fracture plan in the

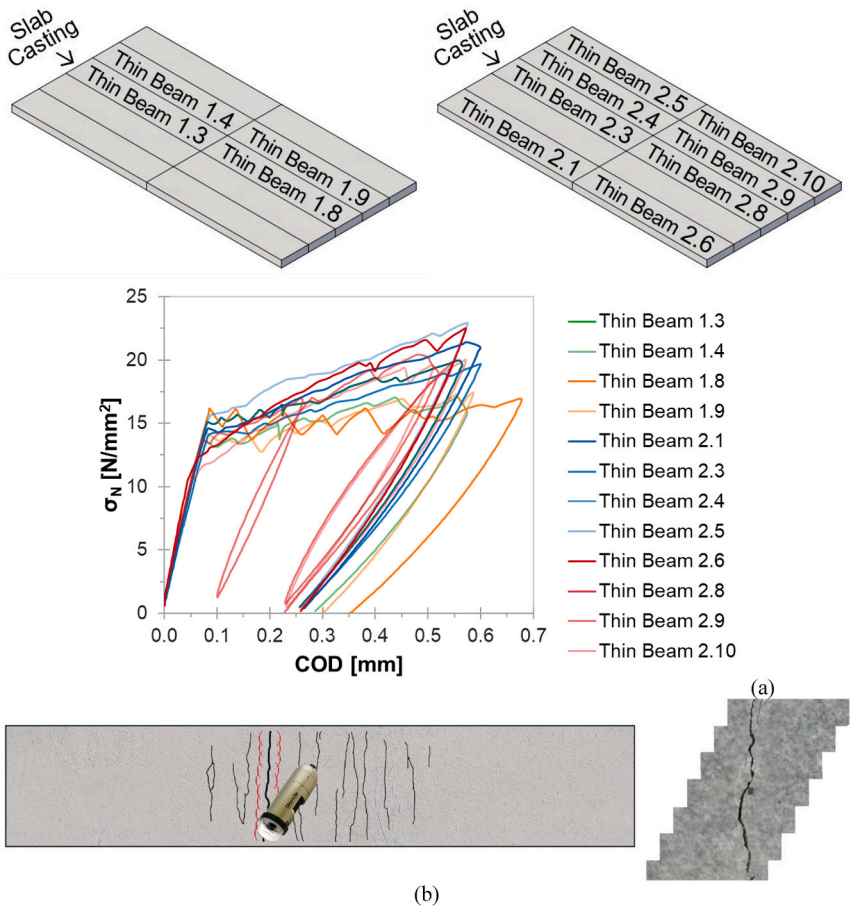

Fig. 10. Pre-cracking flexural nominal stress vs. COD curves (a) and procedure for crack mapping over the width of pre-cracked flexural specimens (b).

DEWS specimens, it was arranged in such a way to have the same fracture plane resulting either parallel or orthogonal to the most likely preferential alignment of the fibres, as driven by the casting flow.

As a matter of fact, the results confirm that in the latter case (*i.e.* fibres orthogonal to the fracture plane) a better tensile response, with higher strength and some kind of strain hardening characteristics, has been obtained, as compared to the former case (*i.e.* fibres parallel to the fracture plane) where a clear strain softening behaviour has been mostly obtained, with far lower strength capacity. Moreover, by relating the measured DEWS test response with the position of the specimen in the original larger cast slab (it is once again worth remarking that DEWS specimens were obtained from the undamaged edge parts of thin beams after having tested them in 4-point bending) the behaviour of specimens "extracted" from those parts of the slab undergoing un undisturbed casting flow always had, in their respective subgroup, a more clear behaviour whether it is a better hardening of a steeper softening.

From the results of DEWS tests a multilinear tensile stress vs. strain constitutive relationship was obtained, as from assumptions shown in Fig. 14, and used as input, through a planar cross-section approach based on force and moment equilibrium equations, to simulate the measured flexural response for both 100 mm deep and 25 mm think beams, whose results shown in Fig. 15 confirm:

- the reliability of the DEWS tests to yield straightforwardly the "constitutive" tensile vs crack-opening response of the investigated category of materials [29];
  −the constitutive law obtained from DEWS tests provides a remarkably good prediction of the flexural response of the tested thin beam specimens, throughout the whole load path. On the other hand, the prediction of the response of 100 mm deep beams is good up to the peak flexural stress but results higher than the experimentally measured one in the post-peak regime. As already explained in Ref. [30] and as also remarked above, the 3D random dispersion of fibres which is likely to be obtained in 100 mm deep beams results into a performance somewhat poorer than the one governed by the planar dispersion of fibres that the 25 mm thickness forces for the 20 mm long fibres in thin beams, and which characterized DEWS specimens as well, which from 25 mm thick beams were obtained.

The parameters of the tensile constitutive law obtained for the material investigated in this study are shown in Table 6 and also compared with the ones proposed in Ref. [30], who also proposed the analysis methodology herein employed, testing a parent mix having an equal composition to the one herein investigated but for the addition of nano-fibres. In the same table typical crack pattern obtained from beams specimens are also shown, together with the average number of cracks are also shown. The effects of a planar 2D dispersion of the fibres in thin beams on the mechanical performance are evident from both the higher peak stress and higher number of cracks, as a result of a more effective stress redistribution action played by the fibres better matching with the stress field.

4.2. *Pre-cracking of specimens*

Fig. 16 shows the response of the beam specimens when undergoing pre-cracking: a good repeatability is highlighted with average residual cumulative Crack Opening Displacement equal to 0.27 mm, which, given the counted average number of cracks equal to 12, corresponds to an average individual crack width equal to 11.4 μm.

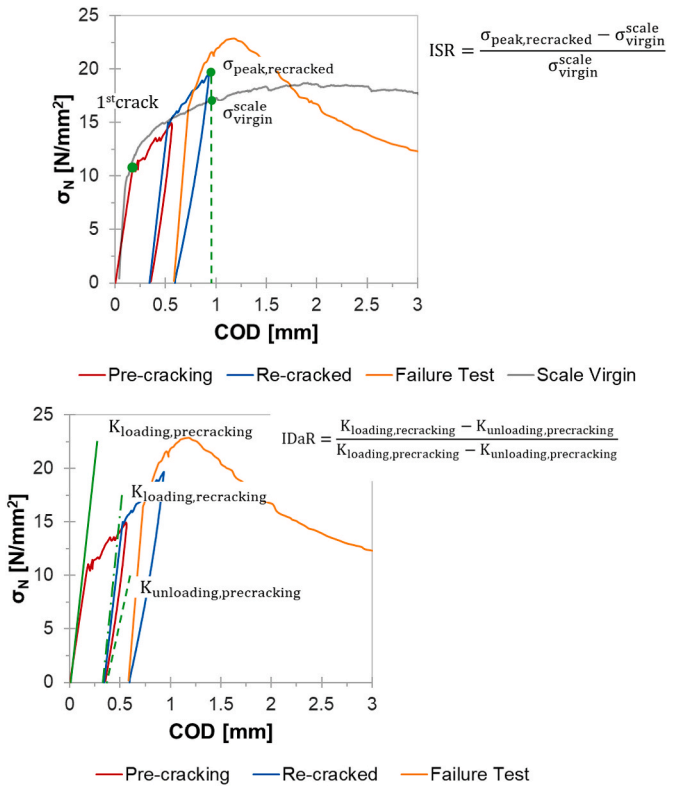

Fig. 11. Schematic and definition of healing indices related to the recovery of stress-capacity (ISR) and stiffness/damage (IDaR).

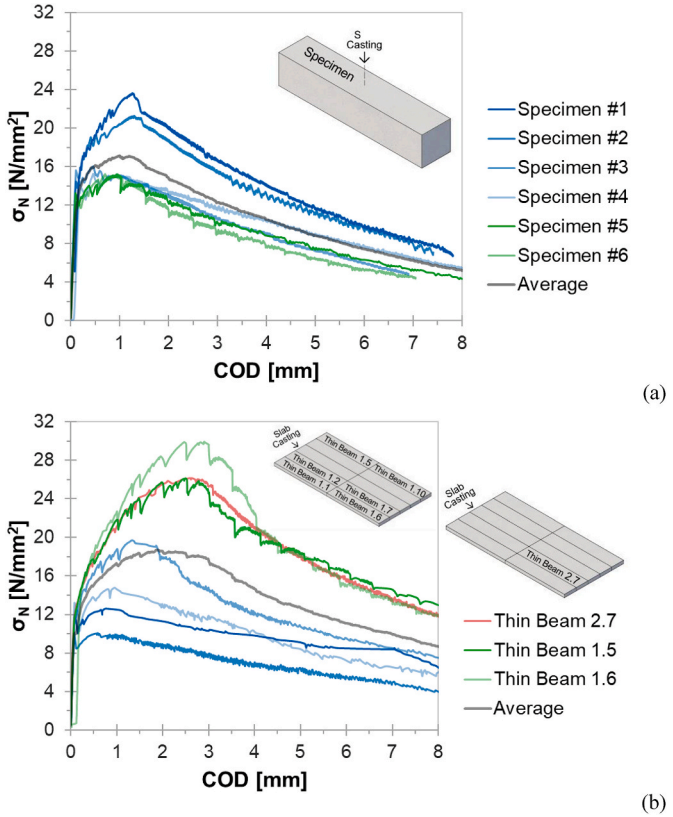

Fig. 12. Nominal flexural stress vs. COD curves from 100 mm deep (a) and 25 mm thick (b) beams tested in four-point bending.

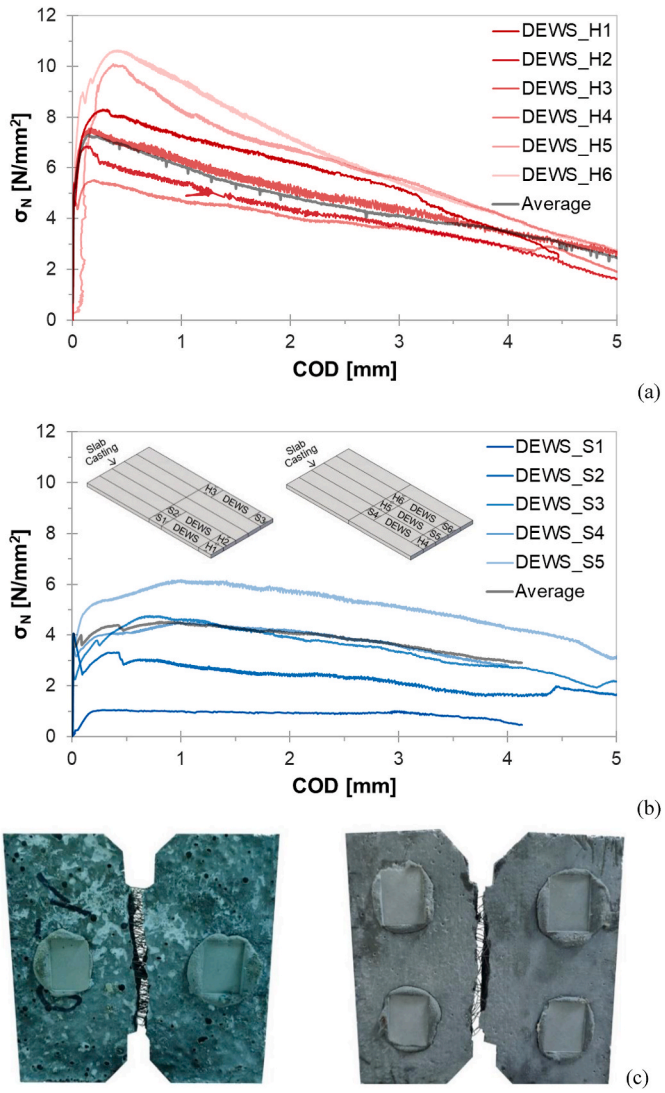

Fig. 13. Tensile strain-hardening vs. softening response of DEWS specimens with fracture plane perpendicular (a) or parallel (b) to casting flow direction with related position of specimens in the. slab casting and different fibre content on ligament section of broken DEWS specimens (c).

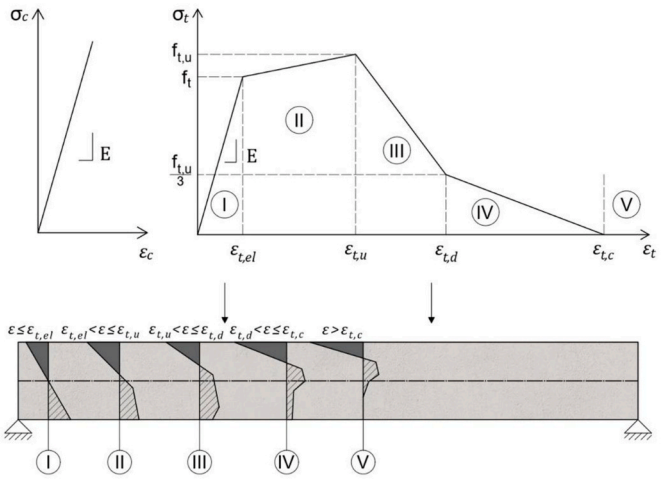

Fig. 14. Compressive and tensile constitutive relationship, as modelled from DEWS test results and cross section evolution stages.

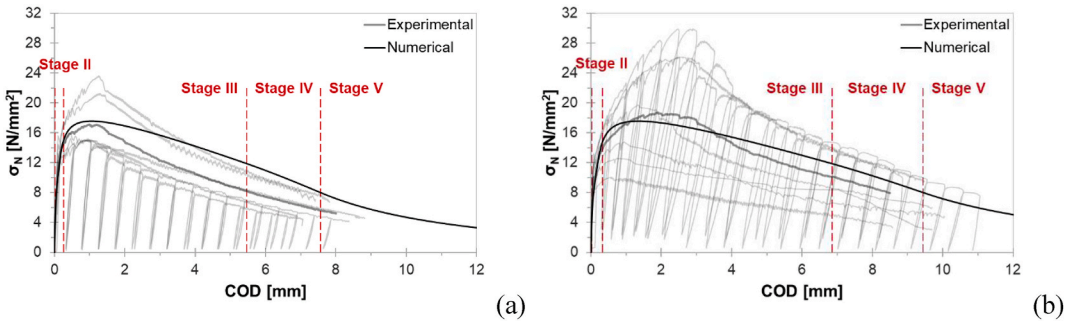

Fig. 15. Experimental 4-point bending test results vs. analytical curves obtained through planar cross section approach employing tensile stress vs. strain constitutive relationship obtained from DEWS tests: deep beams (a) vs. thin beams (b).

Table 6
Experimental average, max and min values of mechanical properties of the mix, and typical cracking patterns in both deep (DB) and thin beams (TB).

parameters	specimens	avg	max	min	crack pattern at the bottom face
σ_{cr} [MPa]	DEWS Parallel	3.5	4.1	2.5	**DB**
f_{ct} [MPa]	DEWS Orthogonal	6.5	9	4.4	
$\sigma_{n,max}$ [MPa]	Deep Beams	17.1	23.6	15.2	
$\sigma_{n,max}$ [MPa]	Thin Beams	19	30	10.1	
crack number	Deep Beams	7	8	6	
crack number	Thin Beams	12	15	9	**TB**
R_c [MPa]	Cubes	136	158	125	

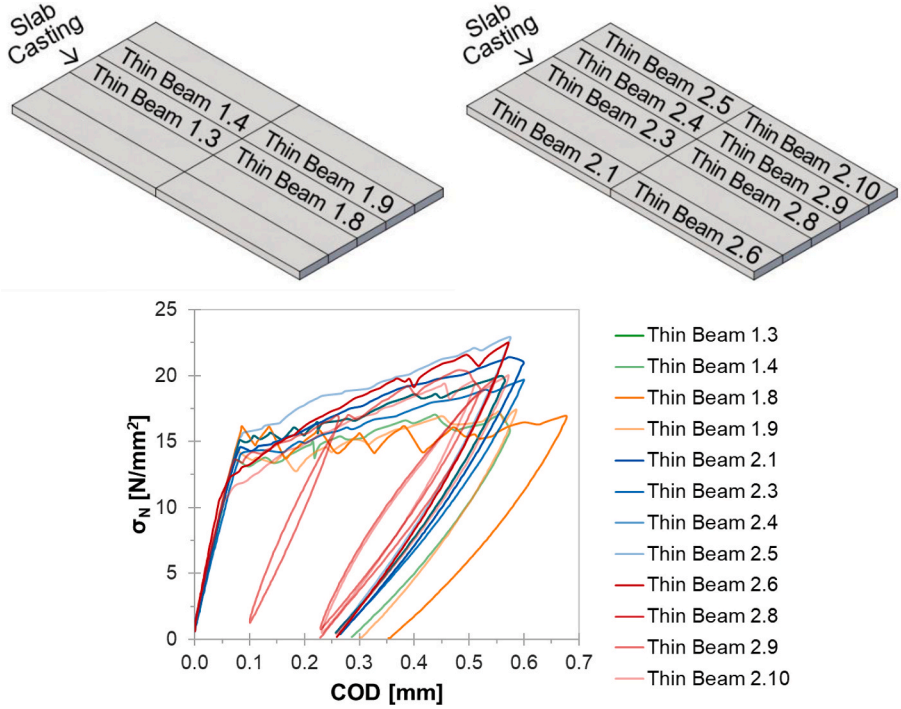

Fig. 16. Pre-cracking nominal flexural stress vs COD curves.

4.3. Crack sealing capacity

The values of the Index of Crack Sealing for the all the tested specimens healed up to two months in the two different aforementioned curing environments is shown in Fig. 17. Interestingly it can be observed that immersion in geothermal water favoured the healing with marginal improvement over the immersion time, which may also be an indicator of the fact that the self-closure of the cracks may effectively counteract any likely degradation mechanism induced by the aggressive substances present in the water, sulphate ions primarily. On the other hand, healing in moist room resulted into lightly worse performance, especially for cracks wider than 15 μm, for which an evident decrease of the crack closure efficiency has been recorded, no matter the duration of the exposure.

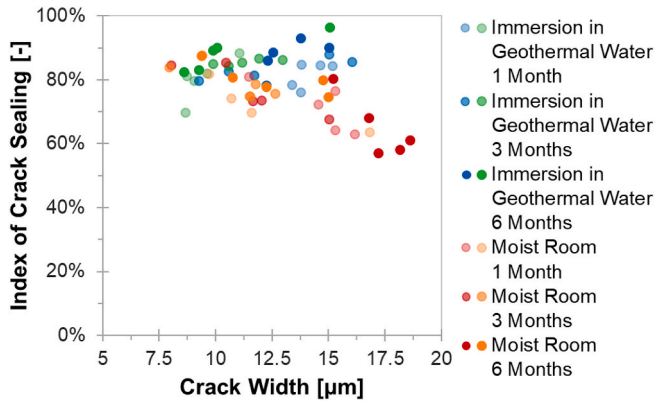

Fig. 17. Index of Crack Sealing vs. initial crack width for different curing times.

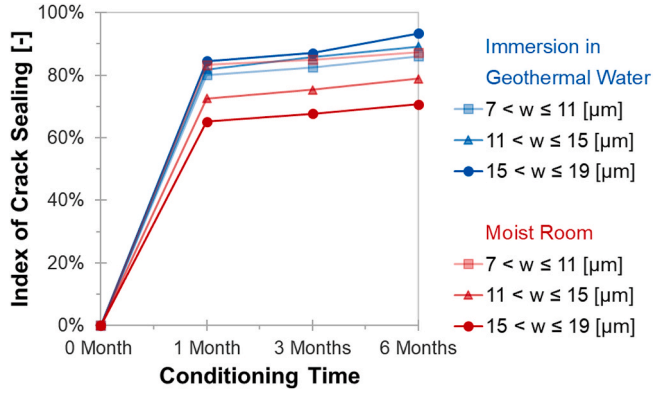

Fig. 18. Evolution of the Index of Crack Sealing vs. time and crack width.

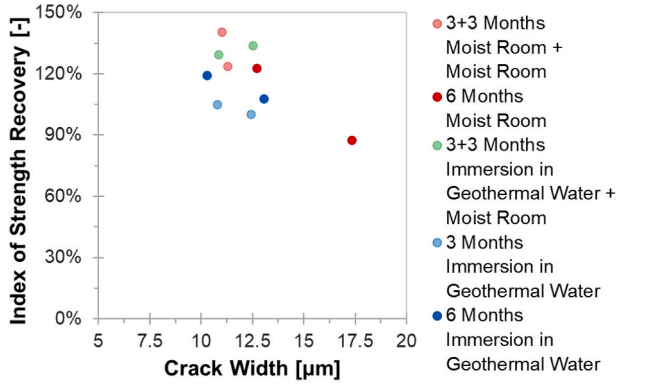

Fig. 19. Index of Strength Recovery for different initial crack widths along healing time.

As a matter of fact, looking into the kinetics of the indices of crack sealing it appears that the closure of the cracks is quite fast, completing its largest share already after one-month exposure (Fig. 18). As already observed by several other authors [35], it is likely that the initial faster healing, by closing down the cracks to a few microns width, prevents any further water or moisture ingress into the same cracks and hence any further progress of the sealing and healing phenomena.

4.4. Self-healing capacity

4.4.1. Recovery of mechanical properties

After three and six months healing the specimens were tested to failure. In this was it was also possible to compare the mechanical

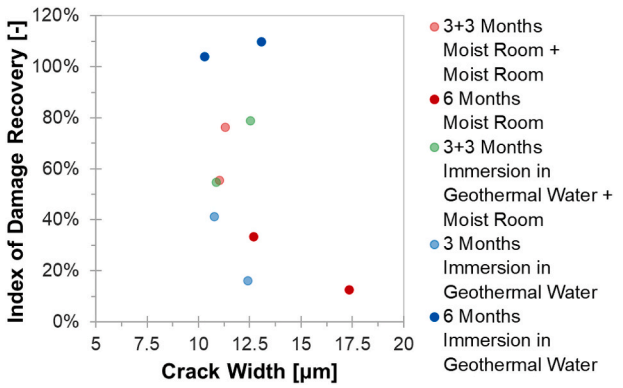

Fig. 20. Index of Stiffness Recovery for different initial crack widths along healing time.

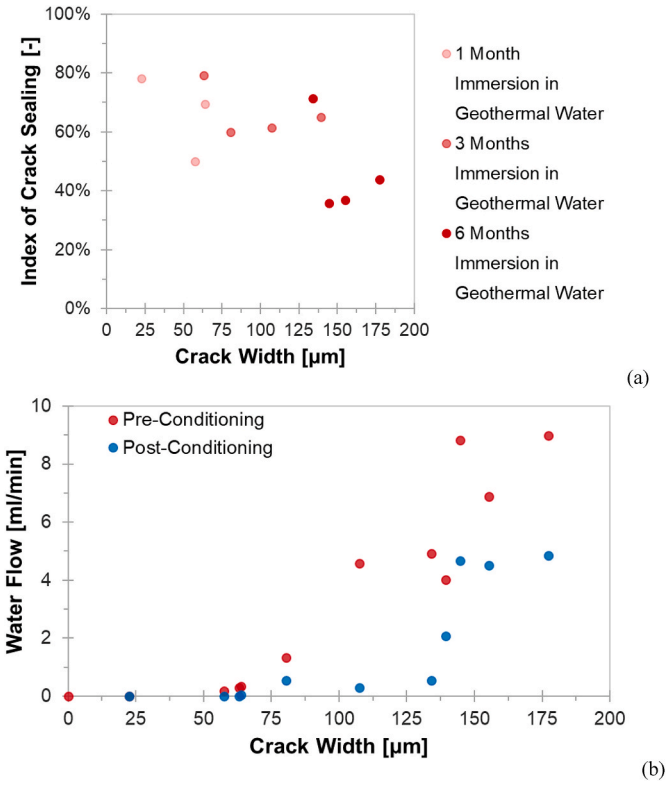

Fig. 21. Index of crack sealing (a) and water flow rate (b) vs. initial crack opening in permeability tests.

performance along the pre-cracking/healing/re-cracking cycles with that of undamaged specimens undergoing the same history (a scaling/homogenization with respect to the first cracking was performed to enable consistent comparison). This comparison allowed the healing induced recovery of the mechanical performance through the calculation of the Indices of Strength Recovery (ISR) and of stiffness/damage recovery (IDaR) calculated as detailed in section 3 and Fig. 11. The calculated values of the ISR shown in Fig. 19 highlight a trend similar to the one already discussed above for the crack sealing. Interestingly, those specimens which after an initial healing period of three months were re-cracked before healing for three further months featured the highest recovery, no matter whether healing occurred under geothermal water or in moist room. This further supports the assumption made above with reference to an initial faster crack-sealing which, closing the crack at the surface level, prevents further ingress of water/moisture inside the specimens which could promote further healing. On the other

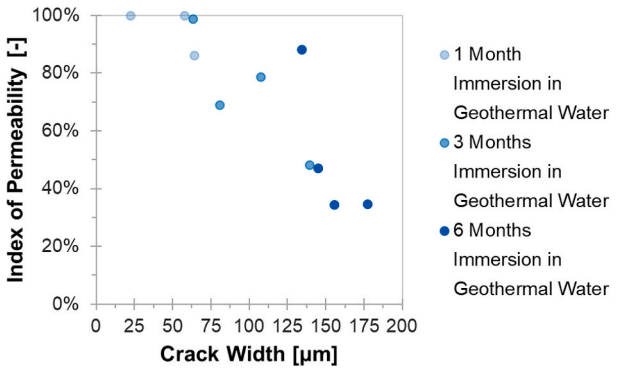

Fig. 22. Index of Permeability Recovery vs. crack width along the healing time.

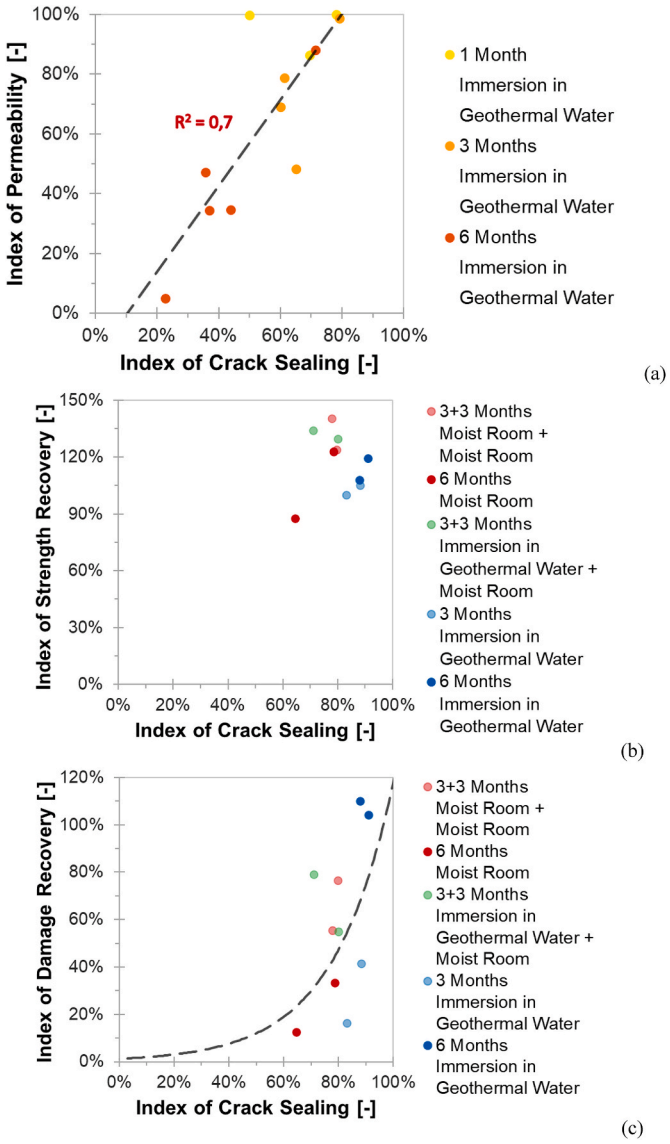

Fig. 23. Correlation between Indices of Recovery of Permeability (a), Strength (b) and Stiffness (c) vs. Index of Crack Sealing.

hand, an intermediate re-cracking, further reopening the partially closed crack, opens the possibility to the healing agent to re-enter the cracked volume and reach deeper freshly cracked surfaces, richer in un-hydrated binder which can thus undergo further delayed hydration.

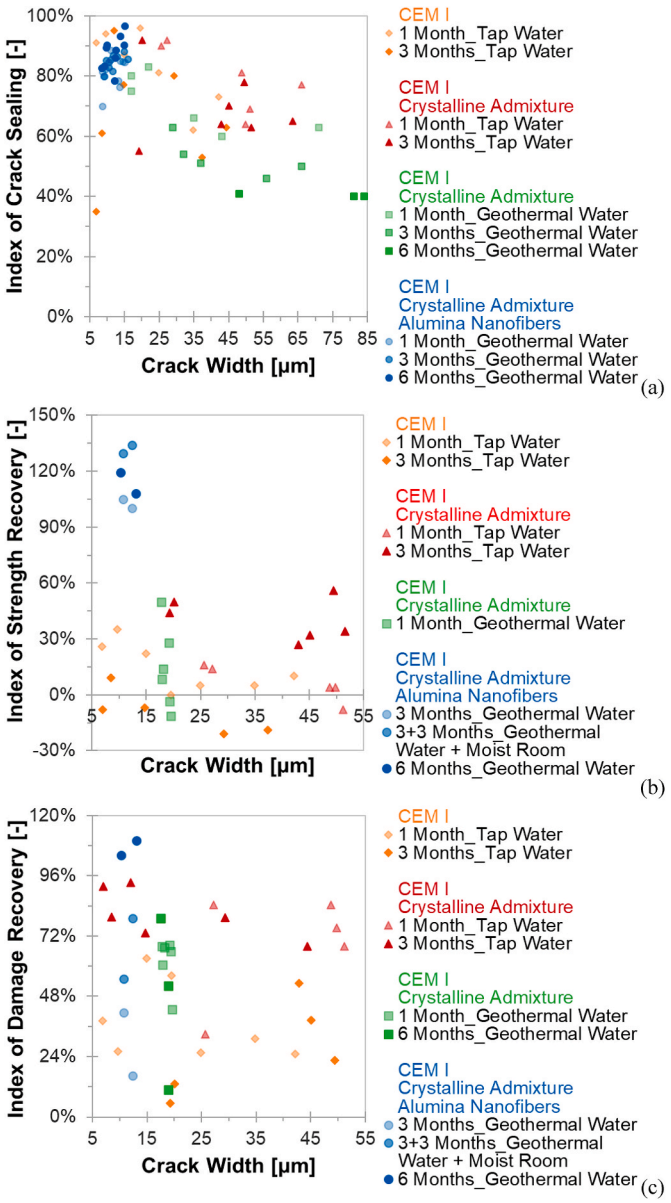

Fig. 24. Correlation between Indices of Recovery of Permeability (a), Strength (b) and Stiffness (c) vs. crack width for different experimental campaigns.

Results quite similar have been obtained for the recovery of the stiffness (Fig. 20), which, in the one hand, proceeded slower than the recovery of the load bearing capacity, coherently also with what observed in other previous studies [30]. Moreover, it seems that this recovery, at least in the case of immersion in water, continued with the immersion time, most likely being also affected by a bulk prolonged hydration of the material throughout the specimen.

4.4.2. *Recovery of (im)permeability*

As said above, specimens for permeability tests were pre-cracked in splitting; visual inspection of cracks after one, three and six months healing in geothermal water resulted into crack sealing shown in Fig. 21, highlighting similar performance as shown and discussed above for specimens employed for the analysis of recovery of mechanical properties.

Results of water flow tests, performed before and after the healing and elaborated in terms of flow rate vs. initial crack opening, as shown in Fig. 22, confirming the known cubic relationship between the two quantities [38]. The change in shape parameters of the correlation curve

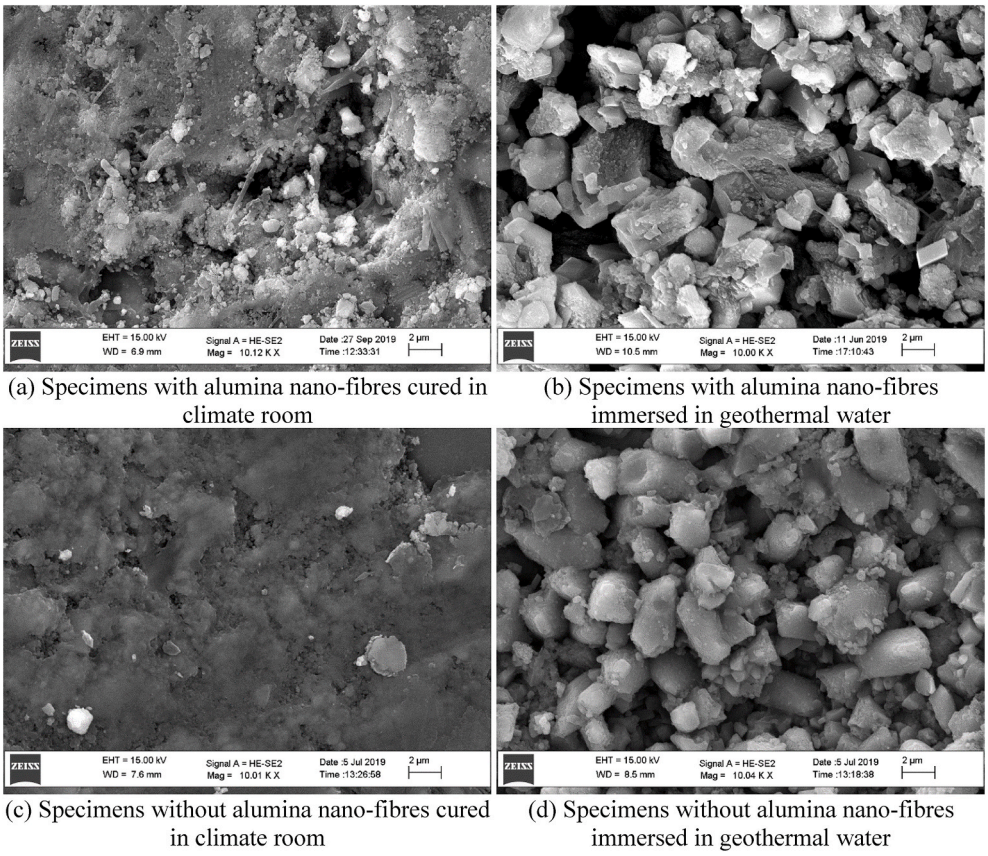

(a) Specimens with alumina nano-fibres cured in climate room

(b) Specimens with alumina nano-fibres immersed in geothermal water

(c) Specimens without alumina nano-fibres cured in climate room

(d) Specimens without alumina nano-fibres immersed in geothermal water

Fig. 25. SEM images of cementitious composites with (a, b) and without (c, d) alumina nano-fibres cured either in climate room (a, c) or in geothermal water (b, d).

before and after the healing for the same crack width brings further support to the assumption that material performance healing is also positively affected by the internal healing of the crack, which obviously a surface microscope inspection does not capture.

The trend of recovery in permeability is shown in Fig. 23, highlighting that a kind of 50 μm threshold for initial crack opening does exist, below which complex 3D sealing of the crack, both at the surface and internally, a complete recovery of the permeability performance can be guaranteed upon short healing time, whereas longer continued healing is needed to heal the material performance in the case of larger cracks.

4.5. Correlation between crack sealing and material performance healing and comparison with other experimental campaigns

In Fig. 23 the Indices of Recovery of mechanical and durability performance are correlated with the crack sealing performance. A good correlation between recovery of (im)permeability and crack sealing confirms the reliability of the measurements.

With reference to the Indices of recovery of mechanical performance, the detected trends are in line with similar findings by the authors' group in previous similar investigations, which highlight as damage recovery needs a crack sealing of at least 60% to start being appreciable, proceeding quite faster for higher sealing rates henceforth. On the other hand, recovery of load bearing capacity, since the pre-cracking and re-cracking occurred in the pre-peak deflection hardening regime, holds stable upon progressive re-closure of the cracks, being also dependent on the crack-sewing effect of the dispersed fibre reinforcement.

The role of alumina nano-fibres can be appreciated by comparing the healing performance as measured in this study and discussed above, with the one measured according to exactly the same methodology on a parent mix equal to the one shown in Table 1 but for the presence of alumina nano-fibres and in case of crystalline admixture. The comparison, shown in Fig. 24, highlights the role of the alumina nano-fibres in promoting a better sealing and even a better healing of the mechanical performance but, most of all, it guarantees that, in the pre-cracking stage, cracks remain within a very narrow opening range. This, as it will also be further elucidated in the next section of this paper, can be due to the synergy between the nano-reinforcement effect provided by the alumina nano-fibres but also by the hydrophilic nature of the same nano-fibres, due to the presence of hydroxyl groups on their surface, which may also make them act as seeds of healing reactions.

4.6. Microstructural analysis

The analysis of the surface morphology was performed with a high-resolution scanning electron microscope (HR-SEM Zeiss Merlin). Measurements were made at an operating voltage of 15 kV. In Fig. 25 SEM images of the micro-structure of the investigated composites after 84 days curing in both environments are shown. The presence of the filaments of alumina nano-fibres is clearly highlighted by the SEM images where their function of reinforcement among the elementary crystal aggregated of the material microstructure is also evident. The influence of continuous availability of water in the geothermal immersion curing environment is evident from a much neater formation of crystals with larger crystals covered by smaller ones, denoting likely continuing development of hydration reactions. This is confirmed by analogue SEM images taken on reference samples made with parent mix without alumina nano-fibres and undergoing the same curing history.

The TG (thermogravimetric) and DTG (Derivative thermogravimetric) curves, shown in Fig. 26, confirm the substantial coincided of the phases of investigated cementitious composites, i.e. portlandite, calcium silicate hydrates and carbonates. The higher peak of carbonate for the mix with alumina nano-fibres, as compared to the parent

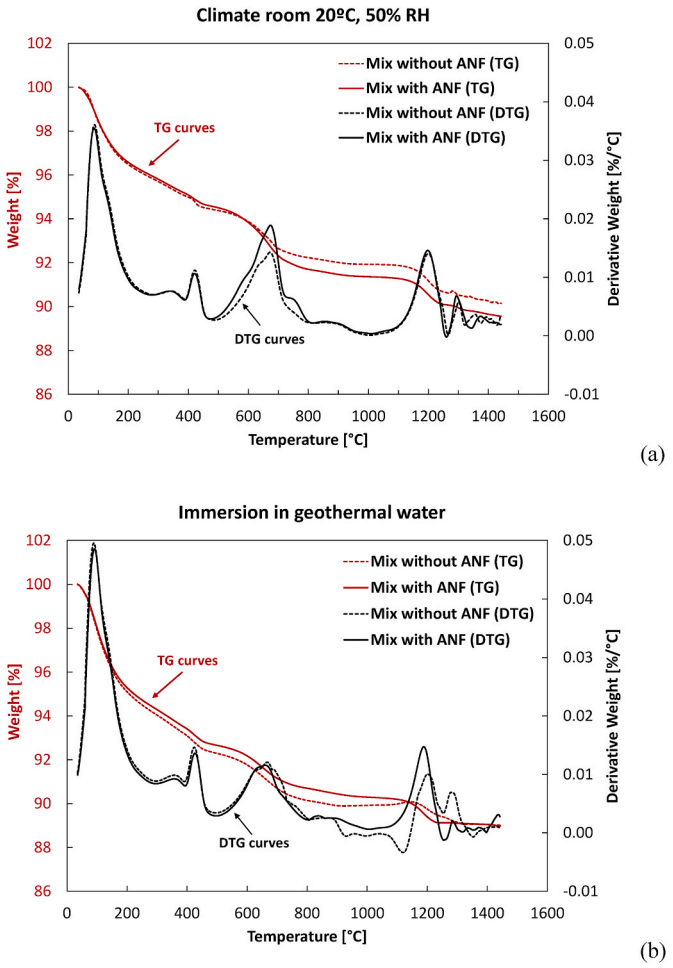

Fig. 26. TG-DTG curves of investigated cured in different regimes: a) 50% RH climate room and b) geothermal water.

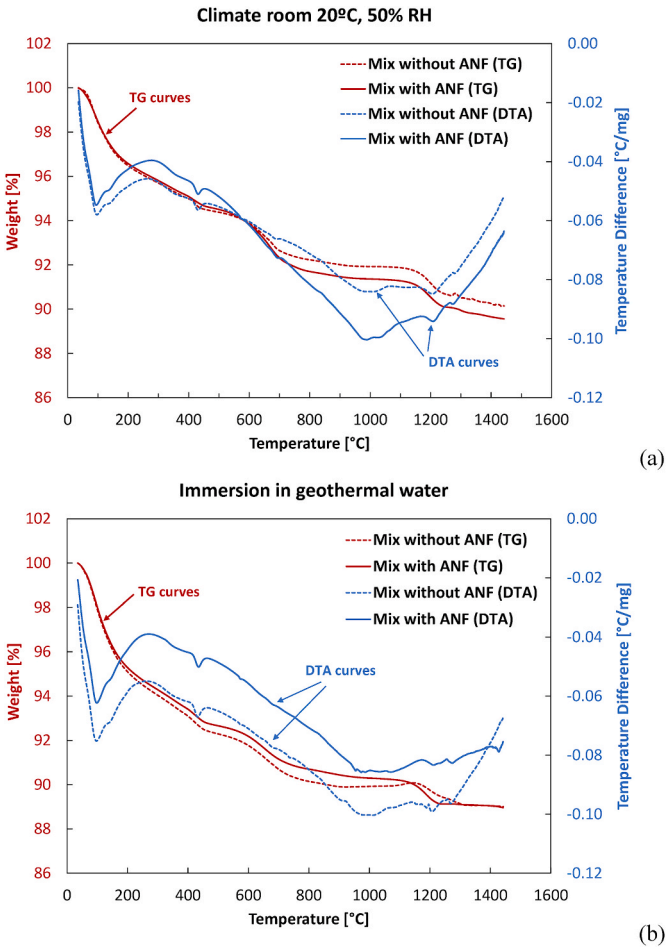

Fig. 27. TG-DTA curves of investigated cured in different regimes: a) 50% RH climate room and b) geothermal water.

reference one, is evident for samples cured in climate room and may be due on the one hand to the availability of carbon dioxide in the air but also to the higher portlandite content available to react with it, due to the hydration fostering reaction role played by the same alumina nano-fibres thanks to their well assessed hydrophilic characteristics [11,25,26].

Fig. 27 shows the TG and DTA curves. The thermograms or Differential Thermal Analysis (DTA curves) represent the temperature difference (in °C/mg) versus temperature (in °C). It should be noted that no exothermic peaks (due to the presence of organic material) were detected in the DTA curves. All the phenomena identified were endothermic due to evaporation or decomposition of the various molecules making up the cementitious composites. Specifically, the endothermic phenomena are clearly visible in the analysed samples and correspond to the weight losses recorded in the TG curves. In particular, there is a strong endotherm at about 100 °C in correspondence with the evaporation of the water and another endotherm, clearly visible, at about 400 °C in correspondence with the decomposition of hydroxides. The endotherm at higher temperatures (700 °C decomposition of carbonates and 1200 °C decomposition of sulphates) are less intense as they are partially covered by an intense phenomenon at about 1000 °C that could be due to the melting of the sample (or part of it) or to a transition.

The X-ray diffraction patterns of the analysed concrete samples are reported in Fig. 28. A qualitative analysis shows the presence of the usual concrete composites such as quartz, ettringite, calcite portlandite, albite and other silicates. Similar crystalline phases have been detected for both mixes, with and without alumina nano-fibres (ANF) and for

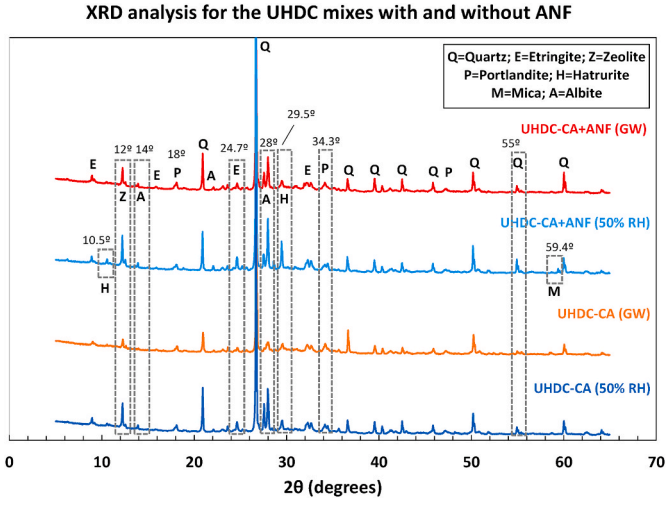

Fig. 28. XRD analysis for the UHDC samples with and without alumina nano-fibres.

both curing conditions (climate room and immersion in geothermal water). The diffraction peaks of portlandite (18°, 34.3° and 47°) and residual ettringite (E) were similar for all the studied cases as can be observed in Fig. 28. It was also detected the presence of quartz and albite, due to the aggregate and slag. The presence of alumina nano-fibres (ANF) does not affect the stability of the hydrated phases since

analogous phases where detected in all the studied diffractograms. Only small differences were observed, for instance the diffraction peaks of ettringite (24.7°) and hatrurite (29.5°) were higher for the samples cured in climate room regardless of the presence of ANF. Moreover, the diffraction peaks of zeolite (12°) and albite (14°) were lower for the sample without ANF immersed in GW. Finally, a diffraction peak of hatrurite at 10.5° and a diffraction peak of mica (59.4°) were only detected for the mix with ANF cured in climate room.

5. Conclusions

The mechanical performance and the autogenous self-healing capacity of an ultra-high performance fibre reinforced cementitious composite, containing alumina nano-fibres and crystalline admixture as self-healing stimulator have been investigated in this paper. The study is meant as a comprehensive study to validate the performance of the mix to be used in one of the pilots of the H2020 ReSHEALience project, *i.e.* a basin for highly chemically aggressive water servicing cooling towers in geothermal power plants. Both flexural and indirect tensile tests have been employed to characterize the mechanical behaviour of the composites, whereas the self-healing performance has been investigated with reference to the recovery of both mechanical performance and water permeability, as indicators of the durability in the cracked state. This latter is meant in a broad sense as the ability of the material to retain its intended level of performance throughout the specified structure service life time-frame.

The main outcomes of this study can be summarized as follows:

- *With reference to the tensile and flexural mechanical behaviour*

The Double Edge Wedge Splitting, employed as an indirect tensile test methodology, is able to yield in a straightforward manner the "constitutive" tensile stress vs. crack opening response of the investigated category of cementitious composites, being further able to discriminate between strain-hardening vs. softening response, as also affected by the flow-induced alignment of the fibres.

- *With reference to the self-healing performance*

The employed multi-test experimental characterization methodology yields consistent results, as shown by the correlation between the recovery of both mechanical and durability properties with the closure of the cracks. Such a cross-comparison of data among different tests is deemed as essential for the definition and calculation of crack-sealing and performance healing indices which can be instrumental to the incorporation of self-healing outcomes into code design provisions in the framework of durability-based design approaches.

- *With reference to the effects of alumina nano-fibres on the overall behaviour of the UHPFRC*

The addition of alumina nano-fibres in the mix, made possible by tailored preparation procedure to achieve the appropriate concentration in the suspension, is likely to yield to a better stress redistribution capacity in the cracked state, as also witnessed by the higher number and thinner width of the cracks which form during the pre-peak stable propagation phase. This, together with the hydrophilic nature of the same fibres which is likely to foster delayed binder hydration reactions, also results into a better and faster healing, in terms of both crack sealing and recovery of mechanical properties, even under exposure to extremely aggressive conditions, like the geothermal water, rich in chlorides and sulphates, investigated in this paper.

The aforementioned findings, while corroborating to enrich the database related to each and all the single topics they refer to, as highlighted in the conclusions, also contribute to validate one of the main assumptions of the overall ReSHEALience project concept, which is the possibility to upgrade, through the pursued "nano-functionalization", the "conventional" UHPFRC concept to the one of a Ultra High Durability Concrete, durability being intended as the capacity of the material and of the structures made of/retrofitted with it, to retain the intended and design-anticipated level of performance throughout the specified structure service life time-frame.

Declaration of competing interest

The authors declare that they have no known competing financial interests or personal relationships that could have appeared to influence the work reported in this paper.

Acknowledgements

The research activity reported in this paper has been performed in the framework of the ReSHEALience project (Rethinking coastal defence and Green-energy Service infrastructures through enHancEd-durAbiLity high-performance cement-based materials) which has received funding from the European Union's Horizon 2020 research and innovation program under grant agreement No 760824. The information and views set out in this publication do not necessarily reflect the official opinion of the European Commission.

The kind collaboration is acknowledged of ReSHEALience partner Penetron Italia in supplying the crystalline self-healing promoter. Kind help of ReSHEALience partner Enel Green Power in allowing visits to geothermal plants in Tuscany for geothermal water supply is also acknowledged. The authors also thank BuzziUnicem, Azichem Ltd. and BASF Italia for supplying of cement, steel fibres and superplasticizer respectively, employed for casting the different investigated UHDC mixes.

The help of Mr. Antonio Cocco and Mr. Paolo Broglia (Laboratory for Testing Materials, Buildings and Structures, Politecnico di Milano) in casting specimens for the experimental programme and providing organizational support for its execution is gratefully acknowledged.

References

[1] K. Sobolev, M. Ferrada Gutierrez, How Nanotechnology can change the concrete world, Am. Ceram. Soc. Bull. 84 (10) (2009) 14–18.
[2] K. Sobolev, I. Flores, R. Hermosillo, L.M. Torres-Martinez, Nanomaterials and nanotechnology for high performance cement composites, in: Proceedings ACI Session on "Nanotechnology of Concrete: Recent Developments and Future Perspectives" November vol. 7, 2006, pp. 91–118. Denver, USA.
[3] K. Sobolev, I. Flores, L.M. Torres-Martinez, P.L. Valdez, E. Zarazua, E.L. Cuellar, Engineering of SiO2 nanoparticles for optimal performance in nano cement-based materials, in: Z. Bittnar, P.J.M. Bartos, J. Němeček, V. Šmilauer, J. Zeman (Eds.), Nanotechnology in Construction 3, Springer, Berlin, Heidelberg, 2009, pp. 139–148.
[4] J. Vera-Agullo, et al., Mortar and concrete reinforced with nanomaterials, in: Z. Bittnar, P.J.M. Bartos, J. Němeček, V. Šmilauer, J. Zeman (Eds.), Nanotechnology in Construction 3, Springer, Berlin, Heidelberg, 2009, pp. 383–388.
[5] Z. Zhao, T. Qi, W. Zhou, D. Hui, C. Xiao, J. Qi, Z. Zheng, Z. Zhao, A review on the properties, reinforcing effects, and commercialization of nanomaterials for cement-based materials, Nanotechnol. Rev. 9 (1) (2020) 303–322.
[6] M.S. Konsta-Gdoutos, Z.S. Metaxa, S.P. Shah, Highly dispersed carbon nanotube reinforced cement based materials, Cement Concr. Res. 40 (7) (2010) 1052–1059.
[7] M.S. Konsta-Gdoutos, G. Batis, P. Danoglidis, E. Zacharopoulou, Effect of CNT and CNF loading and count on the corrosion resistance, conductivity and mechanical properties of nanomodified OPC mortars, Construct. Build. Mater. 147 (2017) 48–57.
[8] A.L. Materazzi, F. Ubertini, A. D'Alessandro, Carbon nanotube cement-based transducers for dynamic sensing of strain, Cement Concr. Compos. 37 (2013) 2–11.
[9] A. D'Alessandro, M. Rallini, F. Ubertini, A.L. Materazzi, J.M. Kenny, Investigations on scalable fabrication procedures for self-sensing carbon nanotube cement-matrix composites for SHM applications, Cement Concr. Compos. 65 (2014) 200–213.
[10] E. Cuenca, S. Rigamonti, E. Gastaldo, L. Ferrara, Crystalline admixture as healing promoter in concrete exposed to chloride-rich environments: experimental study, J. Mater. Civ. Eng. 33 (3) (2021), 04020491, https://doi.org/10.1061/(ASCE)MT.1943-5533.0003604.
[11] E. Cuenca, A. Mezzena, L. Ferrara, Synergy between crystalline admixtures and nano-constituents in enhancing autogenous healing capacity of cementitious

composites under cracking and healing cycles in aggressive waters, Construct. Build. Mater. 266 (2021), 121447.
[12] A. Alatawna, M. Birenoim, R. Nadiv, M. Bozaglo, S. Peretz Damaria, A. Peled, O. Regev, R. Sripada, The effect of compatibility and dimensionality of carbon nanofillers on cement composites, Construct. Build. Mater. 232 (2020) paper 117141.
[13] T.S. Qureshi, D.K. Panesar, Impact of graphene oxide and highly reduced graphene oxide on cement based composites, Construct. Build. Mater. 206 (2019) 71–83.
[14] L. Lu, P. Zhao, Z. Lu, A short discussion on how to effectively use graphene oxide to reinforce cementitious composites, Construct. Build. Mater. 189 (2018) 33–41.
[15] Z. Lu, X. Li, A. Hanif, B. Chen, P. Parthasarathy, J. Yu, Z. Li, Early-age interaction mechanism between the graphene oxide and cement hydrates, Construct. Build. Mater. 152 (2017) 232–239.
[16] Y. Feng, Y.-F. Su, N. Lu, S.P. Shah, Meta concrete: exploring novel functionality of concrete using nanotechnology, Engineered Science (2019), https://doi.org/10.30919/es8d816.
[17] M. Muthu, M. Santhanam, Effect of reduced graphene oxide, alumina and silica nanoparticles on the deterioration characteristics of Portland cement paste exposed to acidic environment, Cement Concr. Compos. 91 (2018) 118–137.
[18] G. Jen, C.P. Ostertag, Resistance to corrosion induced cracking in self consolidating hybrid fiber reinforced concrete, in: G.J. Parra-Montesinos, H.W. Reinhardt, A. E. Naaman (Eds.), High Performance Fiber Reinforced Cement Composites 6, RILEM State of the Art Reports, vol. 2, Springer, Dordrecht, 2012, pp. 163–170.
[19] A.E. Naaman, H.W. Reinhardt, Proposed classification of HPFRC composites based on their tensile response, Mater. Struct. 39 (5) (2006) 547–555.
[20] Perry, V.H. What really is ultra-high performance concrete? – towards a global definition", in C. Shi and B. Chen, eds., Proceedings of the 2nd International Conference on UHPC Materials and Structures, UHPC 2018-China, Fuzhou, China, 7-10 November 2018, RILEM Pubs. S.A.R.L. 89-105.
[21] V.C. Li, C.K.Y. Leung, Steady-state and multiple cracking of short random fiber composites, ASCE. J. Eng. Mech. 118 (11) (1992) 2246–2264.
[22] V.C. Li, D.K. Mishra, H.-C. Wu, Matrix design for pseudo-strain-hardening fibre reinforced cementitious composites, Mater. Struct. 28 (10) (1995) 586–595.
[23] L. Ferrara, P. Bamonte, C.S. Falcó, F. Animato, C. Pascale, A. Tretjakov, E. T. Camacho, P. Deegan, S. Sideri, E.M. Gastaldo Brac, P. Serna, V. Mechtcherine, M.C. Alonso, A. Peled, R.P. Borg, 'An overview on H2020 project "Reshealience"', in: Proceeding IABSE Symposium, Guimaraes 2019: towards a Resilient Built Environment Risk and Asset Management, 2019, pp. 184–191.
[24] Bamonte P., Al Obaidi S., Animato F., Lo Monte F., Mazzantini I., Scalari S. and Ferrara L., "Innovative design concept of cooling water tanks/basins in geothermal power plants using ultra high performance fibre reinforced concrete with enhanced durability", Proceedings of BEFIB2020 RILEM-Fib X International Symposium on Fibre Reinforced Concrete, 21-23 September 2020, Valencia, Spain.
[25] S. Muzenski, I. Flores-Vivian, K. Sobolev, Ultra-high strength cement-based composites designed with aluminum oxide nano-fibers, Construct. Build. Mater. 220 (2019) 177–186.
[26] S. Muzenski, I. Flores-Vivian, K. Sobolev, Hydrophobic modification of ultra-high-performance fiber-reinforced composites with matrices enhanced by aluminum oxide nano-fibers, Construct. Build. Mater. 244 (2020) article 118354.
[27] P. McElroy, H. Emadi, D. Unruh, Permeability and elastic properties assessment of alumina nanofiber (ANF) cementitious composites under simulated wellbore cyclic pressure, Construct. Build. Mater. 239 (2020). Article 117867.
[28] P. Jaishankar, C. Karthikeyan, Characteristics of cement concrete with nano alumina particles, 1, in: IOP Conference Series: Earth and Environmental Science vol. 80, IOP Publishing, 2017. paper 012005.
[29] M. di Prisco, L. Ferrara, M.G.L. Lamperti, Double edge wedge splitting (DEWS): an indirect tension test to identify post-cracking behaviour of fibre reinforced cementitious composites, Mater. Struct. 46 (11) (2013) 1893–1918.
[30] F. Lo Monte, L. Ferrara, Tensile behaviour identification in ultra-high performance fibre reinforced cementitious composites: indirect tension tests and back analysis of flexural test results, Mater. Struct. 53 (6) (2020) 145.
[31] L. Ferrara, N. Ozyurt, M. di Prisco, High mechanical performance of fiber reinforced cementitious composites: the role of "casting-flow" induced fiber orientation, Mater. Struct. 44 (1) (2011) 109–128.
[32] L. Ferrara, M. Faifer, S. Toscani, A magnetic method for non-destructive monitoring of fiber dispersion and orientation in Steel Fiber Reinforced Cementitious Composites - part 1: method calibration, Mater. Struct. 45 (4) (2012) 575–589.
[33] L. Ferrara, M. Faifer, M. Muhaxheri, S. Toscani, A magnetic method for non-destructive monitoring of fiber dispersion and orientation in Steel Fiber Reinforced Cementitious Composites - part 2: correlation to tensile fracture toughness, Mater. Struct. 45 (4) (2012) 591–598.
[34] L. Ferrara, V. Krelani, F. Moretti, M. Roig Flores, P. Serna Ros, Effects of autogenous healing on the recovery of mechanical performance of high performance fibre reinforced cementitious composites (HPFRCCs): part 1, Cement Concr. Compos. 83 (2017) 76–100.
[35] L. Ferrara, V. Krelani, F. Moretti, Autogenous healing on the recovery of mechanical performance of High Performance Fibre Reinforced Cementitious Composites (HPFRCCs): part 2 – correlation between healing of mechanical performance and crack sealing, Cement Concr. Compos. 73 (2016) 299–315.
[36] L. Ferrara, V. Krelani, M. Carsana, A fracture testing based approach to assess crack healing of concrete with and without crystalline admixtures, Construct. Build. Mater. 68 (2014) 515–531.
[37] E. Cuenca, A. Tejedor, L. Ferrara, A methodology to assess crack sealing effectiveness of crystalline admixtures under repeated cracking-healing cycles, Construct. Build. Mater. 179 (2018) 619–632.
[38] L. Ferrara, V. Krelani, F. Moretti, On the use of crystalline admixtures in cement based construction materials: from porosity reducers to promoters of self healing, Smart Mater. Struct. 25 (2016), 084002 (17pp).
[39] E. Cuenca, L. Ferrara, Fracture toughness parameters to assess crack healing capacity of fiber reinforced concrete under repeated cracking-healing cycles', Theor. Appl. Fract. Mech. 106 (2020) 1–12, 102468.
[40] N.M. Bravaya, A.N. Galiullin, S.L. Saratovskikh, A.N. Panin, E.E. Faingol, S. G. Vasil'ev, M.L. Bubnova, V.I. Volkov, Synthesis and properties of hybrid materials obtained by in situ copolymerization of ethylene and propylene in the presence of Al2O3 nanofibers (NAFEN™) on catalytic system rac-Et (2-MeInd) 2ZrMe2/isobutylalumoxane, J. Appl. Polym. Sci. 134 (2017) 44678.
[41] S. Zenille, C.W. Noack, D.A. Dzombak, G.V. Lowry, Characterization of engineered alumina nanofibers and their colloidal properties in water, J. Nanoparticle Res. (2015) 1–14.
[42] R. Ivanov, I. Hussainova, M. Aghayan, M. Drozdova, D. Pérez-Coll, M.A. Rodríguez, F. Rubio-Marcos, Graphene-encapsulated aluminium oxide nanofibers as a novel type of nanofillers for electro-conductive ceramics, J. Eur. Ceram. Soc. 35 (14) (2015) 4017–4021.
[43] D.V. Lebedev, A. Shiverskiy, M. Simunin, V. Solodovnichenko, V. Parfenov, V. Bykanova, S. Khartov, R. Ilya, Preparation and ionic selectivity of carbon-coated alumina nanofiber membranes, Petrol. Chem. 57 (4) (2017) 306–317.
[44] T. Masoud, R. Ivanov, S. Bereznev, S.H. Kazemi, I. Hussainova, Ultra-sensitive voltammetric simultaneous determination of dopamine, uric acid and ascorbic acid based on a graphene-coated alumina electrode, Microchimica Acta 184 (2017) 4603–4610.
[45] Z. Saunders, C.W. Noack, D.A. Dzombak, G.V. Lowry, Characterization of engineered alumina nanofibers and their colloidal properties in water, J. Nanoparticle Res. 17 (2015) 140, https://doi.org/10.1007/s11051-015-2942-4.